

Desilylation Induced by Metal Fluoride Nanocrystals Enables Cleavage Chemistry In Vivo

Dongban Duan, Hao Dong, Zhiyu Tu, Chunhong Wang, Qunfeng Fu, Junyi Chen, Haipeng Zhong, Ping Du, Ling-Dong Sun, and Zhibo Liu*

Cite This: *J. Am. Chem. Soc.* 2021, 143, 2250–2255

Read Online

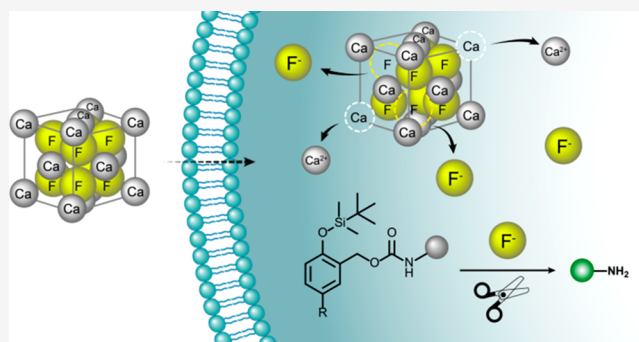
ACCESS |

Metrics & More

Article Recommendations

Supporting Information

ABSTRACT: Metal fluoride nanocrystals are widely used in biomedical studies owing to their unique physicochemical properties. The release of metal ions and fluorides from nanocrystals is intrinsic due to the solubility equilibrium. It used to be considered as a drawback because it is related to the decomposition and defunction of metal fluoride nanocrystals. Many strategies have been developed to stabilize the nanocrystals, and the equilibrium concentrations of fluoride are often <1 mM. Here we make good use of this minimum amount of fluoride and unveil that metal fluoride nanocrystals could effectively induce desilylation cleavage chemistry, enabling controlled release of fluorophores and drug molecules in test tubes, living cells, and tumor-bearing mice. Biocompatible PEG (polyethylene glycol)-coated CaF_2 nanocrystals have been prepared to assay the efficiency of desilylation-induced controlled release of functional molecules. We apply the strategy to a prodrug activation of monomethyl auristatin E (MMAE), showing a remarkable anticancer effect, while side effects are almost negligible. In conclusion, this desilylation-induced cleavage chemistry avails the drawback on empowering metal fluoride nanocrystals with a new function of perturbing or activating for further biological applications.



INTRODUCTION

Metal fluoride nanocrystals (NCs) such as alkaline earth fluorides and rare earth fluorides have been widely used in bioimaging,^{1–4} drug delivery,^{5,6} and biosensing,^{7–9} owing to their unique and advantageous optical, electrical, and magnetic properties.¹⁰ The tunable size and morphology, controllable excitation and emission behaviors, and varied surface modifications make metal fluorides of high relevance in biomedical applications.^{11,12} Ideally, metal fluoride NCs should be chemically stable in water to maintain their structural integrity and optical properties.¹³ However, the release of metal ions and fluoride is intrinsic due to solubility equilibrium, especially under highly diluted or acidic conditions.^{14,15} To protect the metal fluoride NCs from disintegration, various surface coatings have been successfully developed. The decompositions of metal fluoride NCs are often <5% while the equilibrium fluoride concentrations are <1 mM.^{16,17}

Although the dissolution of metal fluoride NCs is undesired, the resulting product fluoride (F^-) could trigger a rapid and efficient desilylation reaction and is commonly used to remove the protecting silyl ether group in organic synthesis.¹⁸ Various silyl ether “caged” fluorescent probes have been successfully developed as fluoride sensors, which could be readily activated by tetrabutylammonium fluoride (TBAF), hydrofluoric acid,

and NaF under aqueous conditions.^{19,20} Recently, our group constructed a bioorthogonal system based on organotrifluoroborate-mediated desilylation and achieved tumor-selective targeting for controlled release of a client protein from the endocytosed nanoparticles.²¹ We wondered whether metal fluoride NCs could also trigger efficient desilylation and if so whether the reaction could be developed into a useful controlled release system, therefore making metal fluoride NCs a perturbing matrix for controlled release of functional molecules. Besides, compared to small molecules such as F^- or a trifluoroborate-derived amino acid for desilylation, metal fluoride NCs may benefit from the enhanced permeability and retention (EPR) effect for tumor targeting and give sustained F^- release for the localized desilylation reaction, empowering metal fluoride NCs to rescue the “function-caged” biomolecules in a tumor-selective manner.

Received: September 29, 2020

Published: February 1, 2021



RESULTS AND DISCUSSION

To pursue this idea, we have developed six model metal fluoride NCs to evaluate their effectiveness for desilylation reaction. Figure 1a shows the transmission electron microscope

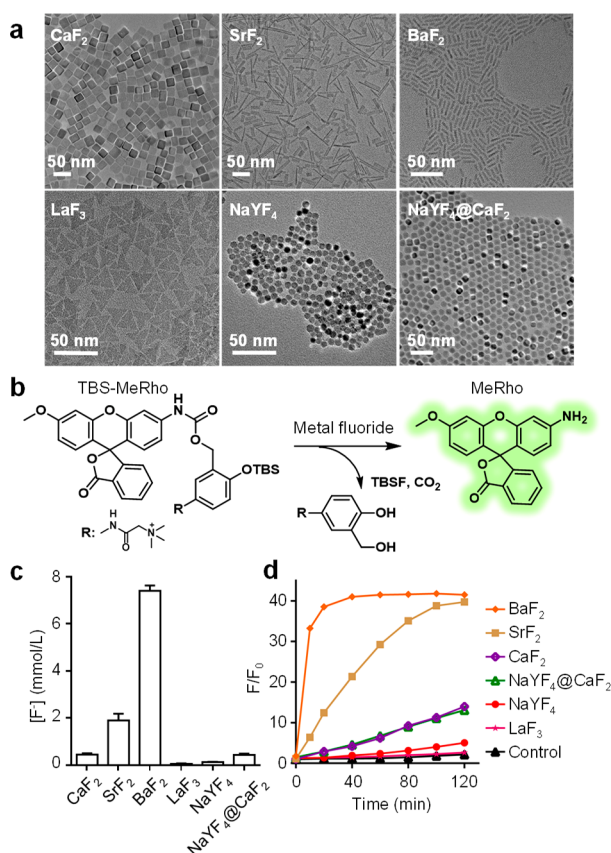


Figure 1. Metal fluoride NCs induced desilylation reaction enabled controlled release of fluorophore under aqueous solution. (a) Representative TEM images of CaF₂, SrF₂, BaF₂, LaF₃, NaYF₄, and NaYF₄@CaF₂ NCs synthesized with thermal decomposition combined with a seed-mediated shell growth strategy.^{16,22,23} All of the metal fluoride NCs exhibit uniform morphology and good monodispersity. To confirm the core-shell structure of NaYF₄@CaF₂ NCs, high-angle annular dark-field scanning transmission electron microscopy and dispersive X-ray spectroscopy line scanning were used, and no separate CaF₂ nanoparticles were observed (Figure S1). The X-ray diffraction (XRD) patterns (Figure S2) suggest that CaF₂, SrF₂, BaF₂, NaYF₄, and NaYF₄@CaF₂ NCs exhibit a face-centered-cubic phase and LaF₃ NCs exhibit a hexagonal phase. These metal fluoride NCs were coated with oleic acid, which are rather lipophilic and easy to aggregate under aqueous conditions. We removed this lipophilic coating by using a ligand exchange method,²⁴ and the resulting metal fluoride NCs are hydrophilic and well-dispersed in water.

(TEM) images of CaF₂, SrF₂, BaF₂, LaF₃, NaYF₄, and NaYF₄@CaF₂ NCs synthesized with thermal decomposition combined with a seed-mediated shell growth strategy.^{16,22,23} All of the metal fluoride NCs exhibit uniform morphology and good monodispersity. To confirm the core-shell structure of NaYF₄@CaF₂ NCs, high-angle annular dark-field scanning transmission electron microscopy and dispersive X-ray spectroscopy line scanning were used, and no separate CaF₂ nanoparticles were observed (Figure S1). The X-ray diffraction (XRD) patterns (Figure S2) suggest that CaF₂, SrF₂, BaF₂, NaYF₄, and NaYF₄@CaF₂ NCs exhibit a face-centered-cubic phase and LaF₃ NCs exhibit a hexagonal phase. These metal fluoride NCs were coated with oleic acid, which are rather lipophilic and easy to aggregate under aqueous conditions. We removed this lipophilic coating by using a ligand exchange method,²⁴ and the resulting metal fluoride NCs are hydrophilic and well-dispersed in water.

As shown in Figure 1c, the equilibrium concentrations of F⁻ were determined by a fluoride electrode and are 0.45, 1.9, 7.4, 0.059, 0.13, and 0.44 mM from 1 mg/mL CaF₂, SrF₂, BaF₂, LaF₃, NaYF₄, and NaYF₄@CaF₂ NCs, respectively. These results corroborate with the solubility of different metal fluoride NCs and are slightly higher than the equilibrium concentrations calculated from *K*_{sp} (solubility product constant) that was measured when they are not nanoscale (Table S1). The greater F⁻ release from nanosized metal fluoride NCs was further verified by comparing the F⁻ release kinetics of CaF₂ of different sizes (Figure S3), which could be explained by the additional surface energy as the particle sizes decrease.^{25,26} It is worth noting that the equilibrium concentrations of F⁻ from CaF₂, SrF₂, BaF₂, and NaYF₄@CaF₂ NCs are >0.44 mmol/L, which are abundant for driving the desilylation reaction. To evaluate the effectiveness of metal fluoride NC induced desilylation, we developed an *ortho*-carbamoylmethylene silyl-phenolic ether system, in which the carbamate carbon is linked to the client molecule MeRho (Figure 1b). Desilylation of this system will trigger the elimination of the carbamate, leading to the breakdown of the amide bond and therefore release the highly fluorescent MeRho. As opposed to the amine-blocked MeRho in the silyl-phenolic ether system, the bright fluorescence of MeRho thus provides a simple and quantitative assay for metal fluoride NC induced desilylation.

The desilylation assays with different metal fluoride NCs were performed under physiological conditions. The increased fluorescence signal from decaged TBS-MeRho was recorded to obtain the kinetic curve for each NC (Figure 1d). As expected, the desilylation reaction rates are highly F⁻-dependent in the order BaF₂ > SrF₂ > CaF₂ ≈ NaYF₄@CaF₂ > NaYF₄ > LaF₃. In addition, the reaction selectivity of desilylation has been investigated by treating TBSO-MeRho with various biologically relevant or corresponding metal ions (1 mM), including Cl⁻, Br⁻, I⁻, BF₄⁻, NO₃⁻, H₂PO₄⁻, Ca²⁺, Sr²⁺, Ba²⁺, La³⁺, and Y³⁺; only the F⁻ ion can efficiently trigger the release of free MeRho (Figure S4), indicating the possibility of using metal fluoride NCs for desilylation reactions in living systems. For the subsequent biological assays, CaF₂ NCs were chosen due to their sufficient desilylation rate and the low toxicity of metal ions in contrast to SrF₂ NCs and BaF₂ NCs.^{27,28}

To achieve better colloidal stability and biocompatibility, CaF₂ NCs were surface-coated by PEG, and the coating was confirmed by FTIR spectroscopy and thermogravimetric analysis (Figures S5 and S6). The hydrodynamic diameter of CaF₂-PEG NCs in different physiological buffers was approximately 65 nm, and the hydrodynamic size of the CaF₂-PEG NCs did not show a notable change in fetal bovine serum (FBS) after 36 h (Figure S7). We also wondered whether the coating would disrupt its dissolution kinetics. As shown in Figure S8, after being diluted from 10 mg/mL to 0.1 mg/mL, the F⁻ concentration in the solution of CaF₂ NCs increased rapidly and reached 100 μM within 1 min, which is enough to accomplish efficient desilylation chemistry *in vivo*.²¹ In fact, PEG coatings will slightly slow down the dissolution, but show a limited impact on the dissolution equilibrium (Figure S9), which corroborates the previous report.²⁵ We have also recorded the dissolution procedure of CaF₂-PEG NCs by TEM. As shown in Figure 2a, after treating CaF₂-PEG NCs (0.1 mg/mL) with acetate buffers (10 mM, pH = 7.4) at 37 °C for 6 h, the cubic morphology gradually transformed

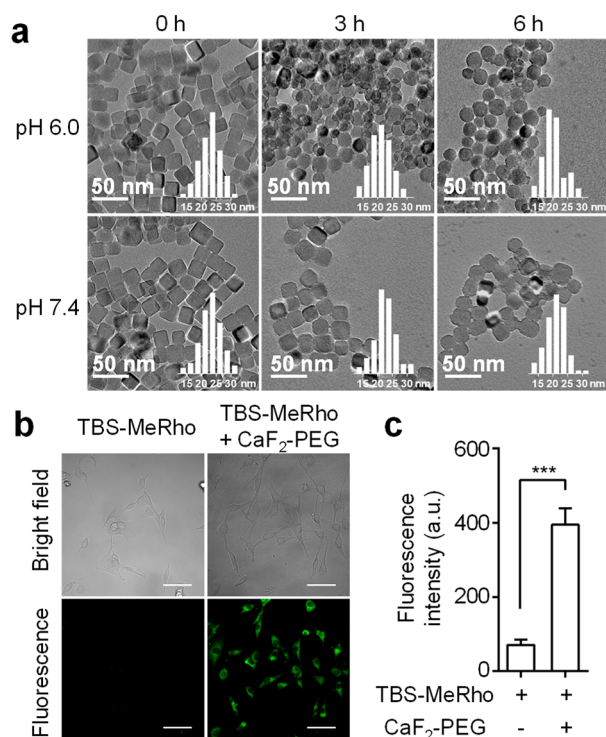


Figure 2. Biocompatible CaF₂-PEG NCs are prepared for desilylation in vitro. (a) TEM images to record the morphology changes of CaF₂-PEG NCs (0.1 mg/mL) in acetate buffers (10 mM, pH = 6.0 or 7.4) at 37 °C. (b) Representative confocal images of U87MG cells after treatment with 0.2 mg/mL CaF₂-PEG NCs, 20 μM TBS-MeRho, or the combination for 4 h. Scale bars, 20 μm. (c) Quantification of the cellular fluorescence intensities with the treatment of CaF₂-PEG NCs or CaF₂-PEG NCs + TBS-MeRho, respectively. The data were collected from the ROIs (*n* = 20) within the cells.

into a sphere and the size of the nanoparticles showed a slight decrease from 23.1 ± 3.2 nm to 22.3 ± 3.3 nm. It was noteworthy that the dissolution was more obvious in acid conditions (pH = 6.0). Almost all cubic NCs transformed into spheres, and the particle size decreased from 22.9 ± 3.1 nm to 20.3 ± 3.6 nm after 6 h of treatment. Moreover, during the degradation process, small-sized residues could be observed in the carbon film and the surface of nanoparticles, which was also observed for CaF₂ NCs without a PEG coating (Figure S10). Given the dissolution kinetics results as mentioned above, we believe that the small-sized residues could be the recrystallized CaF₂ nanoparticles formed after the solution becomes saturated. Collectively, we identified CaF₂-PEG NCs as a sustained F⁻-releasing source which is promising to power the desilylation reaction in a living system.

Before testing the desilylation reactivity of CaF₂-PEG NCs in vitro, the cytotoxicity of CaF₂-PEG NCs has been evaluated systematically. The cell viability was greater than 80% after incubation with 400 μg/mL of CaF₂-PEG NCs for 72 h (Figure S11), proving that CaF₂-PEG NCs were biocompatible in live cells. The cellular uptake of CaF₂-PEG NCs was evaluated by ICP-OES and confocal microscopy (Figure S12). The concentration of calcium in U87MG cells increased over time and reached 12.8 pg/cell after 6 h of incubation. Interestingly, CaF₂-PEG NCs within cells are spherical but not cubic (Figure S13), which could be attributed to the dissolution of CaF₂-PEG NCs in cells.²⁹ The

desilylation reaction was then investigated in a cell-based assay. Cells were incubated with TBS-MeRho and CaF₂-PEG NCs and analyzed by live-cell fluorescence microscopy (Figure 2b). U87MG cells showed a 5.6-fold increase in fluorescence of the entire cell population compared to untreated cells (Figure 2c). The similar experimental results were obtained in BGC823 cells and B16F10 cells (Figure S14). This suggests that CaF₂-PEG NC induced cleavage chemistry remains functional in vitro.

Peptide-drug conjugates (PDCs) hold promise in anti-cancer therapy, but suffer from uncontrolled and inefficient release of the drug.³⁰ We applied CaF₂-PEG NC desilylation to the PDC system. Specifically, the TBS ether-containing carbamate was used to conjugate monomethyl auristatin E (MMAE) to RGD (α_vβ₃ integrin targeting peptide) (Figure 3a). CaF₂-PEG NC incubation caused about 90% MMAE

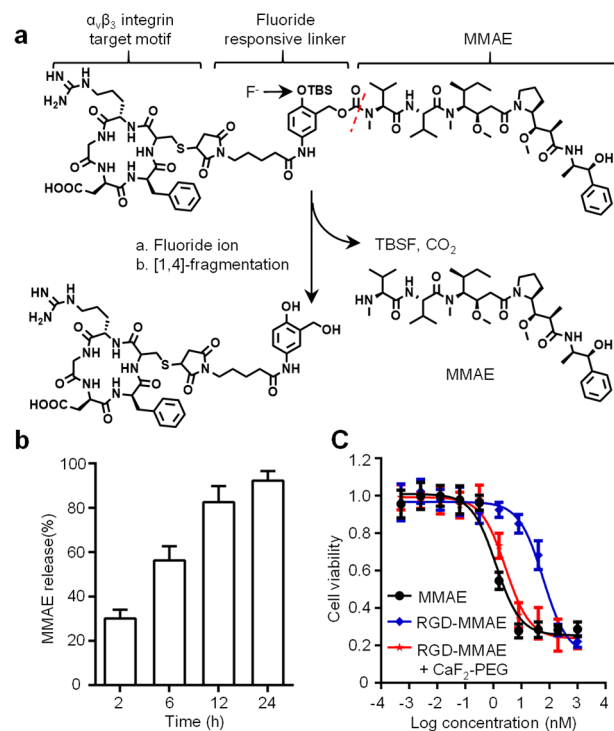


Figure 3. CaF₂-PEG NC desilylation triggered controlled release of drugs and its application to a peptide-drug conjugate. (a) Scheme showing the RGD-MMAE being converted by fluoride into uncaged MMAE. (b) Quantification of the released MMAE from RGD-MMAE (1 μM) after incubation with CaF₂-PEG NCs (0.2 mg/mL) for the indicated time points. (c) Cell viability assays of U87MG cells treated with MMAE, RGD-MMAE, and RGD-MMAE + CaF₂-PEG NCs, respectively (*n* = 5).

release from the RGD-MMAE conjugate (Figure 3b and Figure S15). By treating U87MG cells with RGD-MMAE and CaF₂-PEG NCs, the IC₅₀ of the prodrug showed a 22-fold decrease from 59.6 nM to 2.7 nM, which is close to the potency of MMAE (IC₅₀, 1.3 nM to U87MG cells).³¹ An inhibition assay of tubulin polymerization has been performed that further validated the generation of MMAE from the prodrug (Figure S16).³² By treating U87MG cells with RGD-MMAE only (10 nM) or CaF₂-PEG NCs only (0.2 mg/mL), no significant change of microtubule network was observed, while the treatment of RGD-MMAE+CaF₂-PEG NCs caused substantial disruption to the cellular microtubule network,

causing them to round up into clusters that then underwent apoptosis. Together, these results indicate that RGD–MMAE could be activated effectively by CaF_2 –PEG NCs in vitro.

To accomplish desilylation-mediated controlled release of drugs in the tumor, a selective, intense, and sustainable tumor accumulation of F^- source is essential. ^{18}F NaF positron emission tomography (PET) indicates that blood clearance of free F^- is rapid and mainly through the renal system (Figure S17). The bone uptake is highly intense, which has been well known from the previous reports.^{33,34} In contrast, ^{89}Zr CaF₂–PEG NC PET imaging shows elongated blood circulation and notable tumor accumulation (Figure 4a and Figures S18 and

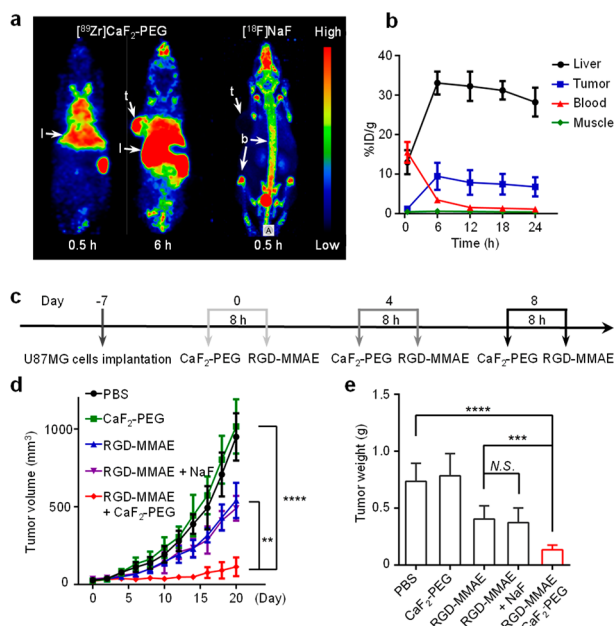


Figure 4. CaF_2 –PEG NCs + RGD–MMAE treatment causes tumor regression in mice. (a) Representative whole-body PET/CT imaging of U87MG tumor-bearing mice at the indicated time points after i.v. administration of 200 μCi of ^{18}F NaF or ^{89}Zr CaF₂–PEG NCs. t, tumor; l, liver; b, bone. (b) Time–activity curve of ^{89}Zr CaF₂–PEG NCs in the liver, blood, tumor, and muscle in mice. (c) Treatment scheme. (d) Tumor growth curves of tumor-bearing mice after the indicated treatments ($n = 6$). (e) Average tumor weight at 20 days after the first treatment (mean \pm s.e.m., $n = 6$).

S19). According to the 3D region-of-interest (ROI) analysis, tumor uptake of ^{89}Zr CaF₂–PEG NCs increases until reaching a plateau of $7.57 \pm 0.71\%$ injected dose per gram (%ID/g), which is >0.3 mg/mL within the tumor at 6 h after tail-vein injection (Figure 4b). As a comparison, 0.1 mg/mL CaF_2 –PEG NCs were used for the aforementioned fluoride release assay (Figure S8), and the fluoride concentration would reach 0.1 mM within 1 min. Although the local fluoride concentration in the tumor might be decreased due to the diffusion, it should be enough to desilylate and activate the MMAE prodrug. Noteworthy, ^{89}Zr CaF₂–PEG NCs exhibit sustained retention in tumors up to 24 h, and the results from an ex vivo biodistribution assay (Figure S18) corroborate with the PET imaging, showing that CaF_2 –PEG NCs could be a sustainable F^- source for desilylation-mediated drug release in tumors.

The treatment efficacy of this prodrug activation system was evaluated on U87MG tumor-bearing mice. In PBS-treated

mice, the volume of U87MG tumors increased by about 20-fold in 20 days (Figure 4d). Upon three rounds of RGD–MMAE + CaF_2 –PEG NC treatments, remarkable tumor shrinkage occurred (Figure 4d). Injection of RGD–MMAE or CaF_2 –PEG NCs alone or RGD–MMAE + NaF did not cause tumor shrinkage. Tumor weight measurements confirmed the antitumor effect caused by desilylation-released MMAE (Figure 4e, Figure S20).

Considering that the release F^- from CaF_2 –PEG NCs might diffuse and liberate prodrugs out of the tumor cells, the biosafety of the treatment has been further evaluated. Mice treated with RGD–MMAE + CaF_2 –PEG NCs did not show significant changes in body weight during the treatment, and almost no tissue damage in the primary organs was observed from histology analysis (Figures S21 and 22). In order to assess whether CaF_2 –PEG NCs would cause any long-term toxicity, a series of experiments including blood chemistry and bone microstructure analysis have been performed (Figures S23 and S24). The parameters of alkaline phosphatase, calcium, and the skeletons of mice treated with CaF_2 –PEG NCs did not significantly change compared with untreated mice. Collectively, these data suggested the promising potential of the CaF_2 –PEG NCs in desilylation-mediated prodrug activation without causing long-term side effects.

CONCLUSIONS

In conclusion, we take CaF_2 NCs as an example to show that the metal fluoride NCs could release adequate F^- to trigger the desilylation chemistry both in vitro and in vivo. The nanometer dimension of metal fluoride NCs enables elongated blood circulation and enhanced tumor permeability compared with small molecules, benefiting persistent tumor treatment. The fluoride NCs should be versatile for all fluoride-containing compounds, especially the less stable fluoride NCs such as biodegradable ones. More importantly, the fluoride NCs can further be functionalized with optical and magnetic properties through doping techniques for imaging-guided theranostics. This work offers exciting opportunities for the design of more intriguing and valuable inorganic–organic prodrugs for on-demand biological applications.

METHODS

Measurement of Fluoride Ion Concentration of Nanosized Metal Fluorides. The metal fluoride NC dispersion (20 mg, 1 mL) was first prepared by sonication for 5 min. The particles were collected from the solution by centrifugation (18000g, 20 min) and dispersed in 20 mL of water. The fluoride-ion-selective electrode (PXSJ-226, Shanghai Precision & Scientific Instrument Inc., Shanghai, China) was immersed in a metal fluoride NC solutions directly. The fluoride ion concentration was obtained by the standardized curve method.

Fluoride Ion Release Kinetics Measured by a Fluoride-Ion-Selective Electrode. The ion release experiments were conducted in a 125 mL plastic beaker containing 100 mL of a 10 mM acetate buffer at 25 °C. A 0.5 mL amount of CaF_2 NCs (20 mg/mL calculated by CaF_2) was added to the medium with stirring, and the fluoride ion concentration (displayed by $-\log[\text{F}^-]$) was measured in situ by the fluoride-ion-selective electrode. The final concentration of CaF_2 was 0.1 mg/mL.

Visual Detection of Disintegration with TEM. The 0.1 mg/mL dilutions of CaF_2 NCs were made with 0.01 M acetate buffer (pH = 6 or pH = 7.4) and incubated with slow shaking at 37 °C. At appropriate time points, a 2 μL droplet of the samples was placed on a lacey carbon film supported on a TEM copper grid, dried at 37 °C, and analyzed with a JEOL JEM-2100 TEM operated at 200 kV.

Prodrug Activation In Vitro. Cells were plated on flat-bottom 96-well plates at a density of 3×10^3 per well. After 12 h of attachment, cells were treated with CaF₂-PEG NCs (0.2 mg/mL), RGD-MMAE (10 nmol/L), or a combination for 72 h before measuring the viability by the CCK8 assay.

Antitumor Efficacy Study. In vivo therapy experiments were performed when the tumor volume reached 50 mm³ in average diameter (7 days after implant). The mice were divided into five groups ($n = 6$). Mice were intravenously injected with CaF₂-PEG NCs (100 mg/kg) or NaF (5 mg/kg) on day 0, 4, and 8, and RGD-MMAE (1 mg/kg) was injected intravenously 8 h later. The mice were monitored for 20 days after treatment. The average and distribution of the weights of the tumors collected from animals in each treatment group were also recorded at the time of sacrifice.

■ ASSOCIATED CONTENT

SI Supporting Information

The Supporting Information is available free of charge at <https://pubs.acs.org/doi/10.1021/jacs.0c10399>.

Experimental details, characterization of organic molecules, supplementary figures (PDF)

■ AUTHOR INFORMATION

Corresponding Author

Zhibo Liu – Beijing National Laboratory for Molecular Sciences, Radiochemistry and Radiation Chemistry Key Laboratory of Fundamental Science, College of Chemistry and Molecular Engineering and Peking-Tsinghua Center for Life Sciences, Peking University, Beijing 100871, China; Beijing Tiantan Hospital, Advanced Innovation Center for Human Brain Protection, Capital Medical University, Beijing 100070, China; orcid.org/0000-0002-5587-4165; Email: zbliu@pku.edu.cn

Authors

Dongban Duan – Beijing National Laboratory for Molecular Sciences, Radiochemistry and Radiation Chemistry Key Laboratory of Fundamental Science, College of Chemistry and Molecular Engineering, Peking University, Beijing 100871, China; orcid.org/0000-0002-1438-0062

Hao Dong – Beijing National Laboratory for Molecular Sciences, State Key Laboratory of Rare Earth Materials Chemistry and Applications, PKU-HKU Joint Laboratory in Rare Earth Materials and Bioinorganic Chemistry, College of Chemistry and Molecular Engineering, Peking University, Beijing 100871, China

Zhiyu Tu – Beijing National Laboratory for Molecular Sciences, Radiochemistry and Radiation Chemistry Key Laboratory of Fundamental Science, College of Chemistry and Molecular Engineering, Peking University, Beijing 100871, China

Chunhong Wang – Beijing National Laboratory for Molecular Sciences, Radiochemistry and Radiation Chemistry Key Laboratory of Fundamental Science, College of Chemistry and Molecular Engineering, Peking University, Beijing 100871, China

Qunfeng Fu – Beijing National Laboratory for Molecular Sciences, Radiochemistry and Radiation Chemistry Key Laboratory of Fundamental Science, College of Chemistry and Molecular Engineering, Peking University, Beijing 100871, China

Junyi Chen – Beijing National Laboratory for Molecular Sciences, Radiochemistry and Radiation Chemistry Key Laboratory of Fundamental Science, College of Chemistry

and Molecular Engineering, Peking University, Beijing 100871, China

Haipeng Zhong – Beijing National Laboratory for Molecular Sciences, Radiochemistry and Radiation Chemistry Key Laboratory of Fundamental Science, College of Chemistry and Molecular Engineering, Peking University, Beijing 100871, China

Ping Du – Beijing National Laboratory for Molecular Sciences, State Key Laboratory of Rare Earth Materials Chemistry and Applications, PKU-HKU Joint Laboratory in Rare Earth Materials and Bioinorganic Chemistry, College of Chemistry and Molecular Engineering, Peking University, Beijing 100871, China

Ling-Dong Sun – Beijing National Laboratory for Molecular Sciences, State Key Laboratory of Rare Earth Materials Chemistry and Applications, PKU-HKU Joint Laboratory in Rare Earth Materials and Bioinorganic Chemistry, College of Chemistry and Molecular Engineering, Peking University, Beijing 100871, China

Complete contact information is available at: <https://pubs.acs.org/10.1021/jacs.0c10399>

Notes

The authors declare no competing financial interest.

■ ACKNOWLEDGMENTS

This work was financially supported by National Natural Science Foundation of China (no. NSFC U1867209 and no. NSFC 21778003) and the Ministry of Science and Technology of the People's Republic of China (2017YFA0506300).

■ REFERENCES

- (1) Prigozhin, M. B.; Maurer, P. C.; Curtis, A. M.; Liu, N.; Wisser, M. D.; Siefe, C.; Tian, B.; Chan, E.; Song, G.; Fischer, S.; Aloni, S.; Ogletree, D. F.; Barnard, E. S.; Joubert, L.-M.; Rao, J.; Alivisatos, A. P.; Macfarlane, R. M.; Cohen, B. E.; Cui, Y.; Dionne, J. A.; Chu, S. Bright sub-20-nm cathodoluminescent nanoprobes for electron microscopy. *Nat. Nanotechnol.* **2019**, *14* (5), 420–425.
- (2) Gargas, D. J.; Chan, E. M.; Ostrowski, A. D.; Aloni, S.; Altoe, M. V. P.; Barnard, E. S.; Sani, B.; Urban, J. J.; Milliron, D. J.; Cohen, B. E.; Schuck, P. J. Engineering bright sub-10-nm upconverting nanocrystals for single-molecule imaging. *Nat. Nanotechnol.* **2014**, *9* (4), 300–305.
- (3) Zhan, Q.; Liu, H.; Wang, B.; Wu, Q.; Pu, R.; Zhou, C.; Huang, B.; Peng, X.; Ågren, H.; He, S. Achieving high-efficiency emission depletion nanoscopy by employing cross relaxation in upconversion nanoparticles. *Nat. Commun.* **2017**, *8* (1), 1058.
- (4) Ashur, I.; Allouche-Arnon, H.; Bar-Shir, A. Calcium Fluoride Nanocrystals: Tracers for In Vivo 19F Magnetic Resonance Imaging. *Angew. Chem., Int. Ed.* **2018**, *57* (25), 7478–7482.
- (5) Ma, P. a.; Xiao, H.; Li, X.; Li, C.; Dai, Y.; Cheng, Z.; Jing, X.; Lin, J. Rational Design of Multifunctional Upconversion Nanocrystals/Polymer Nanocomposites for Cisplatin (IV) Delivery and Biomedical Imaging. *Adv. Mater.* **2013**, *25* (35), 4898–4905.
- (6) Zhang, Y.; Yu, Z.; Li, J.; Ao, Y.; Xue, J.; Zeng, Z.; Yang, X.; Tan, T. T. Y. Ultrasmall-Superbright Neodymium-Upconversion Nanoparticles via Energy Migration Manipulation and Lattice Modification: 808 nm-Activated Drug Release. *ACS Nano* **2017**, *11* (3), 2846–2857.
- (7) Zhao, J.; Gao, J.; Xue, W.; Di, Z.; Xing, H.; Lu, Y.; Li, L. Upconversion Luminescence-Activated DNA Nanodevice for ATP Sensing in Living Cells. *J. Am. Chem. Soc.* **2018**, *140* (2), 578–581.
- (8) Li, H.; Dong, H.; Yu, M.; Liu, C.; Li, Z.; Wei, L.; Sun, L.-D.; Zhang, H. NIR Ratiometric Luminescence Detection of pH Fluctuation in Living Cells with Hemicyanine Derivative-Assembled

Upconversion Nanophosphors. *Anal. Chem.* **2017**, *89* (17), 8863–8869.

(9) Zheng, W.; Zhou, S.; Chen, Z.; Hu, P.; Liu, Y.; Tu, D.; Zhu, H.; Li, R.; Huang, M.; Chen, X. Sub-10 nm Lanthanide-Doped CaF₂ Nanoprobes for Time-Resolved Luminescent Biodetection. *Angew. Chem., Int. Ed.* **2013**, *52* (26), 6671–6676.

(10) Zhou, B.; Shi, B.; Jin, D.; Liu, X. Controlling upconversion nanocrystals for emerging applications. *Nat. Nanotechnol.* **2015**, *10* (11), 924–936.

(11) Dong, H.; Du, S.-R.; Zheng, X.-Y.; Lyu, G.-M.; Sun, L.-D.; Li, L.-D.; Zhang, P.-Z.; Zhang, C.; Yan, C.-H. Lanthanide Nanoparticles: From Design toward Bioimaging and Therapy. *Chem. Rev.* **2015**, *115* (19), 10725–10815.

(12) Chen, G.; Qiu, H.; Prasad, P. N.; Chen, X. Upconversion Nanoparticles: Design, Nanochemistry, and Applications in Therapeutics. *Chem. Rev.* **2014**, *114* (10), 5161–5214.

(13) Lay, A.; Sheppard, O. H.; Siefe, C.; McLellan, C. A.; Mehlenbacher, R. D.; Fischer, S.; Goodman, M. B.; Dionne, J. A. Optically Robust and Biocompatible Mechanosensitive Upconverting Nanoparticles. *ACS Cent. Sci.* **2019**, *5* (7), 1211–1222.

(14) Lahtinen, S.; Lyytikäinen, A.; Pääkkilä, H.; Hömppi, E.; Perälä, N.; Lastusaari, M.; Soukka, T. Disintegration of Hexagonal NaYF₄:Yb³⁺,Er³⁺ Upconverting Nanoparticles in Aqueous Media: The Role of Fluoride in Solubility Equilibrium. *J. Phys. Chem. C* **2017**, *121* (1), 656–665.

(15) Lisjak, D.; Plohl, O.; Vidmar, J.; Majaron, B.; Ponikvar-Svet, M. Dissolution Mechanism of Upconverting AYF₄:Yb,Tm (A = Na or K) Nanoparticles in Aqueous Media. *Langmuir* **2016**, *32* (32), 8222–8229.

(16) Mai, H.-X.; Zhang, Y.-W.; Si, R.; Yan, Z.-G.; Sun, L.-d.; You, L.-P.; Yan, C.-H. High-Quality Sodium Rare-Earth Fluoride Nanocrystals: Controlled Synthesis and Optical Properties. *J. Am. Chem. Soc.* **2006**, *128* (19), 6426–6436.

(17) Estebanez, N.; González-Béjar, M.; Pérez-Prieto, J. Polysulfonate Cappings on Upconversion Nanoparticles Prevent Their Disintegration in Water and Provide Superior Stability in a Highly Acidic Medium. *ACS Omega* **2019**, *4* (2), 3012–3019.

(18) David Crouch, R. Selective monodeprotection of bis-silyl ethers. *Tetrahedron* **2004**, *60* (28), 5833–5871.

(19) Zhou, Y.; Zhang, J. F.; Yoon, J. Fluorescence and Colorimetric Chemosensors for Fluoride-Ion Detection. *Chem. Rev.* **2014**, *114* (10), 5511–5571.

(20) Ke, B.; Chen, W.; Ni, N.; Cheng, Y.; Dai, C.; Dinh, H.; Wang, B. A fluorescent probe for rapid aqueous fluoride detection and cell imaging. *Chem. Commun.* **2013**, *49* (25), 2494–2496.

(21) Wang, Q.; Wang, Y.; Ding, J.; Wang, C.; Zhou, X.; Gao, W.; Huang, H.; Shao, F.; Liu, Z. A bioorthogonal system reveals antitumour immune function of pyroptosis. *Nature* **2020**, *579* (7799), 421–426.

(22) Zhang, Y.-W.; Sun, X.; Si, R.; You, L.-P.; Yan, C.-H. Single-Crystalline and Monodisperse LaF₃ Triangular Nanoplates from a Single-Source Precursor. *J. Am. Chem. Soc.* **2005**, *127* (10), 3260–3261.

(23) Wang, Y.-F.; Sun, L.-D.; Xiao, J.-W.; Feng, W.; Zhou, J.-C.; Shen, J.; Yan, C.-H. Rare-Earth Nanoparticles with Enhanced Upconversion Emission and Suppressed Rare-Earth-Ion Leakage. *Chem. - Eur. J.* **2012**, *18* (18), 5558–5564.

(24) Dong, A.; Ye, X.; Chen, J.; Kang, Y.; Gordon, T.; Kikkawa, J. M.; Murray, C. B. A Generalized Ligand-Exchange Strategy Enabling Sequential Surface Functionalization of Colloidal Nanocrystals. *J. Am. Chem. Soc.* **2011**, *133* (4), 998–1006.

(25) Ma, R.; Levard, C.; Marinakos, S. M.; Cheng, Y.; Liu, J.; Michel, F. M.; Brown, G. E.; Lowry, G. V. Size-Controlled Dissolution of Organic-Coated Silver Nanoparticles. *Environ. Sci. Technol.* **2012**, *46* (2), 752–759.

(26) Zhang, W.; Yao, Y.; Sullivan, N.; Chen, Y. Modeling the Primary Size Effects of Citrate-Coated Silver Nanoparticles on Their Ion Release Kinetics. *Environ. Sci. Technol.* **2011**, *45* (10), 4422–4428.

(27) Pors Nielsen, S. The biological role of strontium. *Bone* **2004**, *35* (3), 583–588.

(28) Kravchenko, J.; Darrah, T. H.; Miller, R. K.; Lyerly, H. K.; Vengosh, A. A review of the health impacts of barium from natural and anthropogenic exposure. *Environ. Geochem. Health* **2014**, *36* (4), 797–814.

(29) Li, R.; Ji, Z.; Dong, J.; Chang, C. H.; Wang, X.; Sun, B.; Wang, M.; Liao, Y.-P.; Zink, J. I.; Nel, A. E.; Xia, T. Enhancing the Imaging and Biosafety of Upconversion Nanoparticles through Phosphonate Coating. *ACS Nano* **2015**, *9* (3), 3293–3306.

(30) Ji, X.; Pan, Z.; Yu, B.; De La Cruz, L. K.; Zheng, Y.; Ke, B.; Wang, B. Click and release: bioorthogonal approaches to “on-demand” activation of prodrugs. *Chem. Soc. Rev.* **2019**, *48* (4), 1077–1094.

(31) Fu, Q.; Li, H.; Duan, D.; Wang, C.; Shen, S.; Ma, H.; Liu, Z. External-Radiation-Induced Local Hydroxylation Enables Remote Release of Functional Molecules in Tumors. *Angew. Chem., Int. Ed.* **2020**, *59* (48), 21546–21552.

(32) Qi, R.; Wang, Y.; Bruno, P. M.; Xiao, H.; Yu, Y.; Li, T.; Lauffer, S.; Wei, W.; Chen, Q.; Kang, X.; Song, H.; Yang, X.; Huang, X.; Detappe, A.; Matulonis, U.; Pepin, D.; Hemann, M. T.; Birrer, M. J.; Ghoroghchian, P. P. Nanoparticle conjugates of a highly potent toxin enhance safety and circumvent platinum resistance in ovarian cancer. *Nat. Commun.* **2017**, *8* (1), 2166.

(33) Li, Y.; Schiepers, C.; Lake, R.; Dadparvar, S.; Berenji, G. R. Clinical utility of 18F-fluoride PET/CT in benign and malignant bone diseases. *Bone* **2012**, *50* (1), 128–139.

(34) Li, C.; Liu, H.; Duan, D.; Zhou, Z.; Liu, Z. Preclinical study of an 18F-labeled glutamine derivative for cancer imaging. *Nucl. Med. Biol.* **2018**, *64–65*, 34–40.